applied sciences

MDPI

Article

Enhanced Adsorption of Methylene Blue in Wastewater Using Natural Zeolite Impregnated with Graphene Oxide

Gabriela Tubon-Usca [1,2], Cyntia Centeno [1], Shirley Pomasqui [1], Amerigo Beneduci [3,*] and Fabian Arias Arias [1,3,*]

[1] Facultad de Ciencias, Escuela Superior Politécnica de Chimborazo (ESPOCH), Riobamba 060155, Ecuador; gabriela.tubon@espoch.edu.ec (G.T.-U.)
[2] Carrera de Ingeniería Química, Grupo de Investigación en Materiales Avanzados (GIMA), Facultad de Ciencias, Escuela Superior Politécnica de Chimborazo (ESPOCH), Riobamba 060155, Ecuador
[3] Department of Chemistry and Chemical Technologies, University of Calabria, Via P. Bucci, Cubo 15D, Arcavacata, 87036 Rende, Italy
* Correspondence: amerigo.beneduci@unical.it (A.B.); fabian.arias@espoch.edu.ec (F.A.A.)

Abstract: The use of graphene oxide (GO) in combination with mesoporous materials has gained interest in the development of adsorbents. In this study, GO was impregnated into zeolite at three concentrations (ZGO2.5, ZGO5, and ZGO10) through a simple thermal process to enhance the adsorption of methylene blue (MB). Characterization of the resulting materials was performed using spectroscopic techniques such as UV-Vis and FT-IR spectroscopy, SEM, and EDS, confirming the presence of GO on zeolite. Batch experiments were conducted to evaluate their performance, analyzing contact time, pH effect, and adsorption kinetics. Pseudo-first-order, pseudo-second-order, and Elovich kinetic models were applied, and the adsorption mechanism was studied using Langmuir, Freundlich, Temkin II, and Dubinin–Radushkevich (D-R) isotherms at different temperatures. Optimal adsorption was achieved at 273 K, 100 mg L^{-1} of MB, adsorbent mass of 100 mg, 250 rpm, and pH 5–9, with 90% removal efficiency after 70 min. The pseudo-second-order, Freundlich, and D-R models best described the process ($R^2 > 0.98$), suggesting a mixed physisorption–chemisorption mechanism. The maximum adsorption capacity from the D-R isotherm reached 119 mg g^{-1} at 333 K. Thermodynamic studies showed that adsorption was a spontaneous and endothermic process. These findings highlight the potential of GO-impregnated zeolite as an effective adsorbent for MB.

Keywords: graphene oxide; zeolite; methylene blue; adsorption kinetics; thermodynamic studies

check for updates

Academic Editor: Jens Ejbye Schmidt

Received: 4 February 2025
Revised: 1 March 2025
Accepted: 2 March 2025
Published: 5 March 2025

Citation: Tubon-Usca, G.; Centeno, C.; Pomasqui, S.; Beneduci, A.; Arias, F.A. Enhanced Adsorption of Methylene Blue in Wastewater Using Natural Zeolite Impregnated with Graphene Oxide. *Appl. Sci.* **2025**, *15*, 2824. https://doi.org/10.3390/app15052824

Copyright: © 2025 by the authors. Licensee MDPI, Basel, Switzerland. This article is an open access article distributed under the terms and conditions of the Creative Commons Attribution (CC BY) license (https://creativecommons.org/licenses/by/4.0/).

1. Introduction

Nowadays, water quality is a global concern. As a result, clean water is a central focus of the Sustainable Development Goals (SDGs), specifically SDG 6, i.e., Clean Water and Sanitation. This goal aims to ensure access to safe drinking water for all, which is essential for public health, environmental sustainability, and economic growth [1]. However, in recent years, the development of the textile industry has been strengthened due to the increase in the so-called fast fashion, which has caused an impact on the environment due to the large amounts of water used in the different stages of production [2]. Many dyes used in textile production contain toxic chemicals such as formaldehyde, phthalates, azo dyes, and alkylphenols, along with heavy metals like lead, mercury, and cadmium. These pollutants contaminate rivers, soils, and ecosystems, posing serious risks to communities.

The most common dye in the industry is methylene blue (MB) (3,7-bis(dimethylamino) phenothiazine chloride tetra methylthionine chloride). It is a synthetic cationic dye widely used in the textile, pharmaceutical, plastics, paper printing, and food industries [3]. The MB dye is a very stable molecule soluble in water and alcohol, not degradable under natural conditions; the persistent presence of this dye even in low concentrations (<1 ppm) harms the ecosystem, causing health alterations [4,5]. MB exposure can lead to serious side effects including eye burns that may cause permanent damage and skin irritation, and its ingestion may induce symptoms such as vomiting, diarrhea, gastrointestinal irritation, shock, and mental confusion [6]. Given its high toxicity, especially compared to anionic dyes, managing and removing MB from industrial effluents is a critical environmental concern to prevent harm to both humans and aquatic life. Conventional wastewater treatment to remove dyes employs a variety of physical and chemical methods [7]. The physical methods include sedimentation, coagulation, filtration, ion exchange, adsorption, and reverse osmosis [4–6,8]. On the other hand, the chemical methods include oxidation, ozonation, photochemical degradation, and electrochemistry [9,10]. The adsorption method as an alternative for the removal of methylene blue has been widely studied in recent years due to its high yields and accessibility, and the development and functionalization of new materials has improved the capacity to remove contaminants from water and wastewater [3,5,6,11,12]. The effectiveness of adsorption depends on the strategic selection of precursor materials and the optimized design of the adsorbent. An ideal material should have a high surface area, well-defined porosity, specific functional groups, and a robust structure to maximize its retention capacity. Additionally, it must be abundant, cost-effective, insoluble, environmentally friendly, non-toxic, and easily regenerable [6]. In the search for adsorbents with these characteristics, numerous researchers have developed and studied materials such as activated carbon, clays, biomaterials, and zeolites [4,11,13–19].

Zeolites have emerged as crucial players in wastewater dye removal due to their natural abundance, relatively low synthesis cost, unique structural features, and advantageous surface properties. These characteristics closely align with the key requirements of an ideal adsorbent, positioning zeolites as highly effective materials for wastewater treatment [18,20]. The development of zeolite composites with enhanced adsorption capacity has been the focus of recent studies. Among the materials investigated are zeolite NaA [21], MFI zeolite nanosheets [19], MZA/RGO [22], and M-ZP [23], which have demonstrated improved adsorption and ion exchange properties and, thus, increased effectiveness in removing water contaminants.

Zeolites are crystalline aluminosilicates with a well-defined porous structure, which can be either synthetically produced or naturally mined. Their unique crystalline structure, composed of interconnected AlO_4 and SiO_4 tetrahedra, forms a network of micropores with a size range from 0.3 to 1 nm [24], providing a large specific surface area and excellent cation exchange capacity [18]. Over 50 natural zeolite minerals have been identified, of which analcime, chabazite, clinoptilolite, heulandite, natrolite, phillipsite, and stilbite occur in significant quantities [24]. Clinoptilolite, one of the most abundant zeolites on earth, has a 2D channel system featuring two parallel channels (a 10-membered ring of 7.2 Å × 4.4 Å and an 8-membered ring of 4.7 Å × 4.1 Å) intersecting with a third 8-membered ring channel (5.5 Å × 4.0 Å) [23,25]. Its framework consists of SiO_4 and AlO_4 tetrahedra with charge-balancing cations (Na^+, K^+, Ca^{2+}, Mg^{2+}) [25]. It is commonly employed in wastewater treatment, though it exhibits limited adsorption efficiency for cationic contaminants [22]. This limitation is attributed to its low ion exchange capacity, intrinsic to its crystalline structure with a Si/Al ratio generally ranging from 4 to 6. Since the above alkaline and earth alkaline cations affect its adsorption capacity, acid treatments can be used to reduce

its cation content, thereby improving the adsorption capacity [26]. However, they can generate hazardous waste that poses a significant threat to the environment.

On the other hand, graphene oxide has shown promising results as an adsorbent for pollutant removal due to its high adsorption capacity. This capacity is attributed to its exceptional physicochemical properties, such as its large specific surface area and the presence of various oxygen-containing functional groups in its structure [27]. The Hummers method, introduced in the 1950s, remains one of the most widely used techniques for synthesizing graphene oxide (GO) [28]. This process involves the strong oxidation of graphite in a highly concentrated acidic medium, using a reactive mixture of sulfuric acid, potassium permanganate, and hydrogen peroxide [29]. This oxidation introduces oxygenated functional groups (carboxyl, hydroxyl, and epoxy groups) into the graphene structure, facilitating its exfoliation into monolayers or few-layered sheets [30]. However, the corrosive and toxic nature of the reagents employed generates harmful gases and ionic waste, posing a significant environmental concern. To address this environmental challenge, we previously reported [31] a scalable and environmentally friendly method for producing GO, suitable for industrial-scale water treatment.

The integration of graphene oxide with other materials has proven to be a highly effective strategy for enhancing its adsorption capacity [22,32]. This improvement arises from the synergy between the complementary properties of the different components, resulting in composite materials with optimized physical and chemical characteristics. Specifically, the combination with porous materials, such as silica or activated carbons, significantly increases the available surface area, thereby enhancing the adsorption capacity for contaminants [11,22,33]. Different materials can exhibit varied adsorption mechanisms (physical, chemical, or ion exchange), allowing for a more efficient interaction with a broader range of contaminants. Furthermore, the functionalization of graphene oxide through the addition of specific functional groups or the incorporation of other materials can fine-tune the adsorbent's selectivity towards certain dyes or metals. Additionally, these combinations can improve the chemical and mechanical stability of the adsorbent, increasing its durability and facilitating its reuse [34,35].

This research aims to enhance the adsorption capacity of clinoptilolite zeolite by combining it with graphene oxide, a material known for its high adsorption capacity. This process leads to the formation of zeolite–graphene oxide nanocomposites, synthesized hydrothermally to improve the material's surface area and ion exchange capacity. The obtained nanocomposites are characterized using spectroscopic techniques (UV-Vis and FT-IR spectroscopy, BET technique, SEM, EDS), and their adsorption capacity is evaluated through batch experiments.

2. Materials and Methods

2.1. Materials

All materials were used as received. Graphite powder (<20 μm, 99%, CAS 7782-42-5) was purchased from Sigma–Aldrich Laborchemikalien GmbH, St. Louis, MO, USA. Sulfuric acid (H_2SO_4, 95.0–98.0%), hydrochloric acid (HCl, 37.0%, CAS 7647-01-0), potassium permanganate ($KMnO_4$, >98.0%), and hydrogen peroxide (H_2O_2, CAS 7722-84-1) were obtained from Merck (Rahway, NJ, USA). Natural zeolite (clinoptilolite, 85–95% purity, 14–40 mesh) was supplied by Watprosa S.A. (Quito, Ecuador).

2.2. Preparation of Graphene Oxide

In a typical experiment to obtain graphene oxide, the synthesis was carried out based on [31] with some modifications, aiming to create a simple and effective process. Three grams of graphite powder was introduced into a reaction flask, followed by the addition

of 70 mL of concentrated sulfuric acid (H_2SO_4). The mixture was subjected to vigorous stirring throughout the process. Subsequently, 9 g of potassium permanganate ($KMnO_4$) was added gradually and with caution to prevent the reactor temperature from exceeding 20° C, which was maintained using an ice bath. After 45 min, the reaction mixture was transferred to an oil bath preheated to 50 °C, and the temperature of the solution was maintained below 50 °C for an additional 30 min under vigorous stirring. Thereafter, 150 mL of distilled water was added dropwise, increasing the temperature to 90 °C and maintaining it for another 20 min. Subsequently, 500 mL of distilled water was added, followed by the slow dropwise addition of 15 mL of hydrogen peroxide (H_2O_2). At this stage, the color of the solution transitioned from dark brown to yellowish, indicating the formation of a graphite oxide suspension, which was washed with a 1:10 HCl solution. The precipitate was further washed with distilled water several times, each for 15 min, by means of centrifugation at 3000 rpm, until achieving a neutral pH (of approximately 6). The precipitated material was recovered and dried at 90 °C for 24 h.

2.3. Preparation of Impregnated Zeolite and Graphene Oxide Composites

Three graphene oxide suspensions with concentrations of 2.5 mg mL^{-1}, 5 mg mL^{-1}, and 10 mg mL^{-1} were prepared from the recovered material. Subsequently through a simple thermal process, 1 g of zeolite was added to each suspension and submitted to a sonication process for 30 min. The mixture was then subjected to magnetic stirring at 200 rpm under controlled conditions, at 70 °C for 4 h. Finally, the nanocomposites were dried at 50 °C for 24 h. The prepared nanocomposites were named ZGO2.5, ZGO5, and ZGO10. Each nanocomposite was characterized by FTIR, UV–visible spectroscopy, and scanning electron microscopy (SEM).

2.4. Point of Zero Charge (PZC)

The pH of the point of zero charge (pH_{PZC}) experiments was determined through a Hanna 22001 potentiometer with temperature control.

A series of five 50 mL conical flasks were each charged with 20 mL of a 0.1 M sodium chloride solution prepared in ultrapure, nitrogen-purged water. The pH of each solution was adjusted to a specific value within the range of 2 to 10 using 0.1 M HCl and 0.1 M NaOH solutions. Then, 25 milligrams of ZGO10 was added to each flask, and the mixtures were stirred at a rate of 250 rpm for 12 h. The final pH of each solution was measured and plotted against the initial pH (pH drift method) [36]. The point at which the curve intersected the line representing equal initial and final pH values was the point of zero charge (pHpzc) of the material adsorbent, according to the procedures previously described by Riva and coworkers [37].

2.5. Solution Preparation

Analytical-grade reagents were used for all adsorption experiments. A 1000 mg L^{-1} MB solution was prepared in ultrapure water (18.3 MΩ·cm). Standard working solutions were used in the tests through serial dilutions. The pH of the solutions was adjusted using 0.1 N NaOH and HCl solutions and measured using a pH meter (HI221, from Hanna Instruments, Woonsocket, RI, USA).

2.6. Adsorption Kinetics and Individual Material Adsorption Capacity

The contact time and adsorption kinetics of graphene oxide (GO) and zeolite were studied to determine their individual MB adsorption capacities. All adsorption investigations were carried out in triplicate. In 250 mL Erlenmeyer flasks, 100 mL of a 100 mg L^{-1} MB solution was mixed with 100 mg of the adsorbent material. The mixture was stirred at 250 rpm. Aliquots were taken every 3 min for the first 60 min, then every 10 min until

180 min. MB concentration in each sample was analyzed by UV-vis spectroscopy. This procedure was repeated for the ZGO2.5, ZGO5, and ZGO10 composites. The effect of pH on MB adsorption was investigated using a batch test. The procedure was similar to the one described above, with the MB solution pH adjusted from 2 to 10 using 0.1 N NaOH and HCl solutions. Adsorption isotherm experiments were conducted at different temperatures (298 K, 303 K, 313 K, and 333 K) using 10 mL of solutions at concentrations of 10, 25, 50, 75, 100, 250, 500, and 1000 mg L^{-1}. Adsorption was studied using a batch test at a fixed pH of 6.5, using 10 mg of the nanocomposites. Methylene blue adsorption capacity (*qt*), defined as the amount of adsorbed MB per unit mass of adsorbent, was determined using the following equation [5,38]

$$qt = \frac{(C_0 - C_e)V}{W} \quad (1)$$

where C_0 (mg g^{-1}) and Ce (mg L^{-1}) are the initial and final methylene blue concentrations, respectively. *V* (L) is the volume of the methylene blue solution, and W (g) is the mass of the nanocomposite. In the adsorption equilibrium conditions, Ct = Ce and qt = qe. Ce is the equilibrium concentration, and qe denotes the equilibrium adsorption capacity. The removal efficiency (RE%) of the nanocomposite can be calculated as follows:

$$RE\% = \frac{(C_0 - C_e)}{C_0} \times 100 \quad (2)$$

2.7. Characterization

The composites were characterized by Uv–visible spectroscopy using a UV-vis spectrophotometer (Thermo Scientific, Evolution 220, Waltham, MA, USA), in the wavelength range from 190 nm to 800 nm. For the analysis of natural zeolite, zeolite was sonicated for 15 min in ultrapure water, then the supernatant was analyzed over a wavelength range from 190 nm to 800 nm [39]. Subsequently, an aqueous solution of GO was prepared at a 1 mg mL^{-1} concentration and further diluted for the UV–visible analysis. Finally, all nanocomposites (ZGO2.5, ZGO5, and ZGO10) were sonicated in the same way as zeolite, and then their UV–visible spectra were obtained. The FTIR analysis was carried out using the Fourier transform infrared spectrometer Jasco FT/IR-4000 (Easton, MD, USA). The structure and surface morphology were determined on a scanning electron microscope (SEM, JSM-IT100 InTouchScope, JEOL, Musashino, Akishima, Tokyo, Japan) equipped with a JEOL-made electron-dispersive X-ray spectrometer (EDS) with accelerating voltage of 9 kV and 12 kV.

3. Results and Discussion

3.1. Synthesis and Characterization

3.1.1. UV–Visible Characterizations

GO was synthesized using the modified Hummers method for the subsequent impregnation of natural zeolite. The initial material was analyzed using a UV–visible spectrophotometer in aqueous solution for the characterization and identification of its characteristic spectrum.

The UV-Vis spectrum of graphene oxide (GO), shown in Figure 1a, indicated that the predominant absorption peaks were localized at a wavelength of 234 nm, corresponding to the $\pi - \pi *$ transitions of the aromatic C=C bond. Furthermore, a small shoulder at 301 nm was identified, attributed to the $n - \pi *$ transition of the C=O bond, explained by the presence of carboxylic groups in GO, in accordance with previously reported studies [29,31,40].

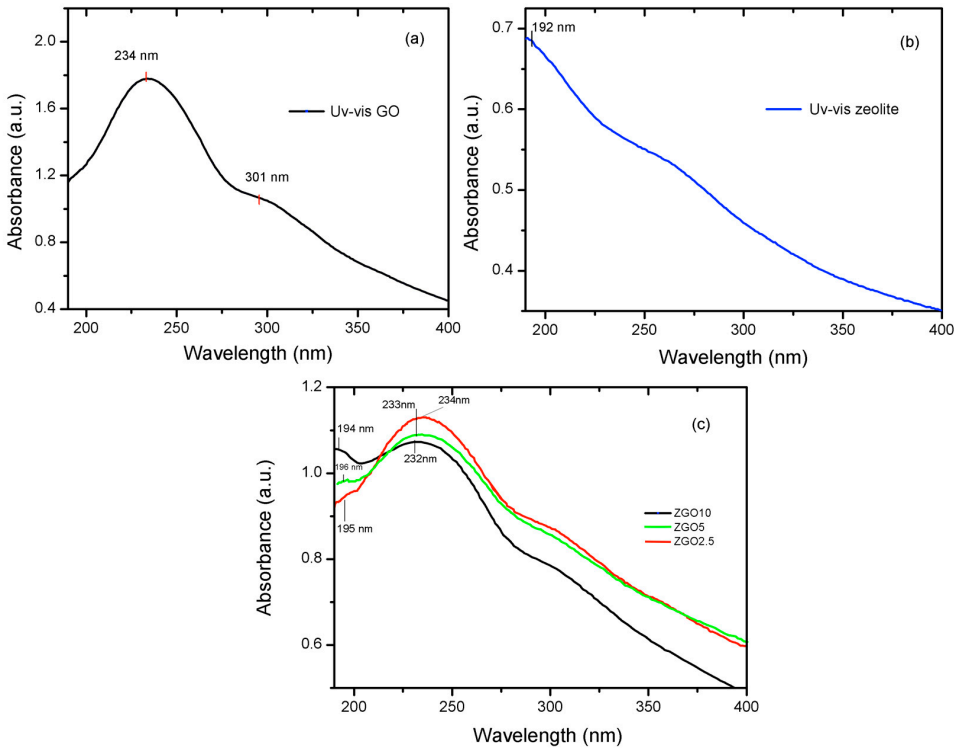


Figure 1. (**a**) Uv–visible spectrum of graphene oxide; (**b**) Uv–visible spectrum of natural zeolite; (**c**) spectra of natural zeolite impregnated with GO at a concentration of 10 mg mL^{-1} (ZGO10), 5 mg mL^{-1} (ZGO5), and 2.5 mg mL^{-1} (ZGO2.5); all spectra were recorded in aqueous solution.

The spectrum depicted in Figure 1b belongs to natural zeolite; here, a peak appears at 192 nm corresponding to $n - \sigma^*$ electronic transitions involving the oxygen–silicon charge transfer, specifically (O^{2-} ® Si^{4+}) transitions, within the SiO_2 tetrahedral framework. This indicates that the framework predominantly consisted of Si—O—Si bonds with minimal Al substitution, which exhibit higher charge transfer energy compared to Si—O—Al bonds. This fact explains the high-energy transitions occurring in the deep UV region.

Regarding the impregnated composite, Figure 1c shows the spectra of zeolite impregnated with graphene oxide (ZGO2.5, ZGO5, and ZGO10). A peak is visible at 196 nm, 192 nm, and 194 nm, respectively, corresponding to the n−σ* transition, as explained above for the zeolite spectrum (Figure 1b). The peaks at 194 nm and 196 nm underwent a slight redshift compared to those in the natural zeolite spectrum. Meanwhile, the peaks located at 233, 234, and 232 nm correspond to the GO $\pi - \pi *$ transitions of the aromatic C=C bond. Additionally, a shoulder around 300 nm is present, identifying the $n - \pi *$ transition of the C=O bond.

3.1.2. FTIR Characterizations

The FTIR spectra presented in Figure 2 illustrate the characteristic vibrational modes of graphene oxide (GO), natural zeolite, and the synthesized GO–zeolite composites (ZGO2.5, ZGO5, and ZGO10). The GO spectrum (green) exhibits a broad peak at 3359 cm^{-1}, corresponding to hydroxyl (O–H) groups and adsorbed water molecules within the GO interlayers. The peak at 1720 cm^{-1} is attributed to carboxyl groups, while the absorption at 1631 cm^{-1} corresponds to aromatic C=C stretching vibrations, characteristic of sp^2-hybridized carbon domains. Additionally, ether (C–O) groups are observed at 1034 cm^{-1} and 1061 cm^{-1}, confirming the presence of oxygen-containing functional groups that enhance GO hydrophilic properties [29,32,41,42]. The FTIR spectrum of natural zeolite (pink) displays a broad absorption band at 3483 cm^{-1}, associated with O–H stretching vibrations

from the hydroxyl groups. The peak at 1627 cm^{-1} is linked to the bending vibrations of water molecules coordinated with Na^+ and Ca^{2+} ions in the zeolite framework. The strong band at 1021 cm^{-1} corresponds to Si–O–Si stretching vibrations, which are indicative of the presence of silicate tetrahedra. The peak at 788 cm^{-1} represents the symmetric stretching of Si–O–Si bonds, confirming a well-ordered crystalline structure typical of clinoptilolite zeolites [43,44]. The spectra of the nanocomposite materials (blue, red, and black) exhibited similarities, with variations primarily due to the interaction between GO and zeolite. O–H stretching vibrations are present at 3417 cm^{-1}, 3400 cm^{-1}, and 3395 cm^{-1}, corresponding to the contributions of the hydroxyl groups from both zeolite and GO. The characteristic C=C vibrations of GO, initially at 1631 cm^{-1}, appear shifted slightly to 1629 cm^{-1} and 1627 cm^{-1}, indicating possible interactions between the GO functional groups and the zeolite framework. This small redshift (~4 cm^{-1}) suggests electron density alterations in sp^2 carbon domains, likely due to weak interactions such as hydrogen bonding or Van der Waals forces. Additionally, the peaks at 1028 cm^{-1} and 1040 cm^{-1} in the composite spectra correspond to aromatic carbon ring vibrations, confirming the presence of benzene-like structures from GO. The peak at 789 cm^{-1}, initially present in the natural zeolite spectrum, experienced a redshift, indicating no significant structural disruption in the zeolite framework but rather surface-level interactions with GO.

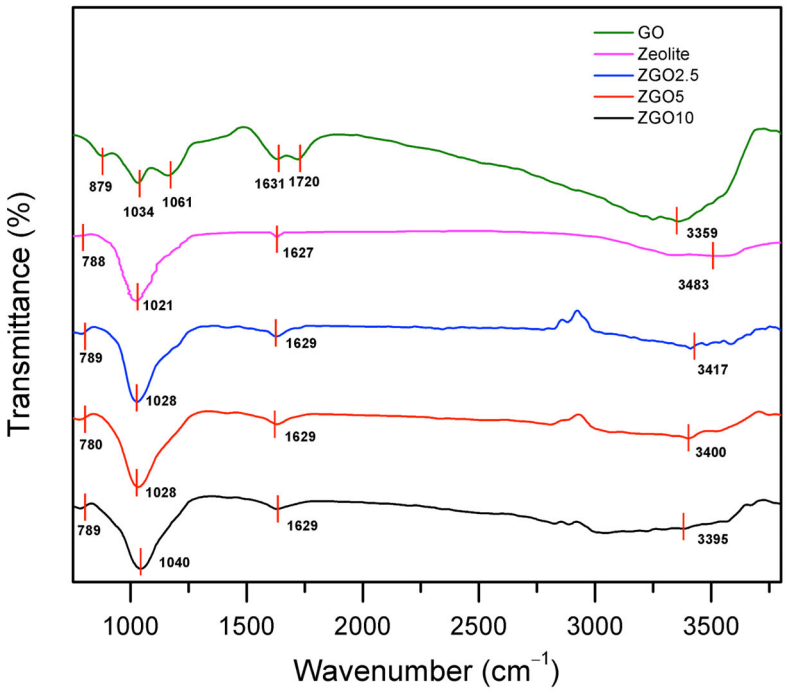


Figure 2. FTIR spectra of GO, zeolite, and the ZGO2.5, ZGO5, and ZGO10 nanocomposites.

3.1.3. SEM Characterizations

The morphology of GO, zeolite, and the nanocomposites was analyzed using scanning electron microscopy (SEM). Figure 3a displays a micrograph of GO, revealing layers exceeding 10 µm in size, arranged as wrinkled veils stacked atop one another. This wrinkled appearance is a distinctive characteristic of GO, resulting from the presence of functional groups that induce deformation as they strive to achieve electronic configuration stability. Additionally, this feature signifies a transition from sp^2 to sp^3 hybridization, highlighting structural changes in the material.

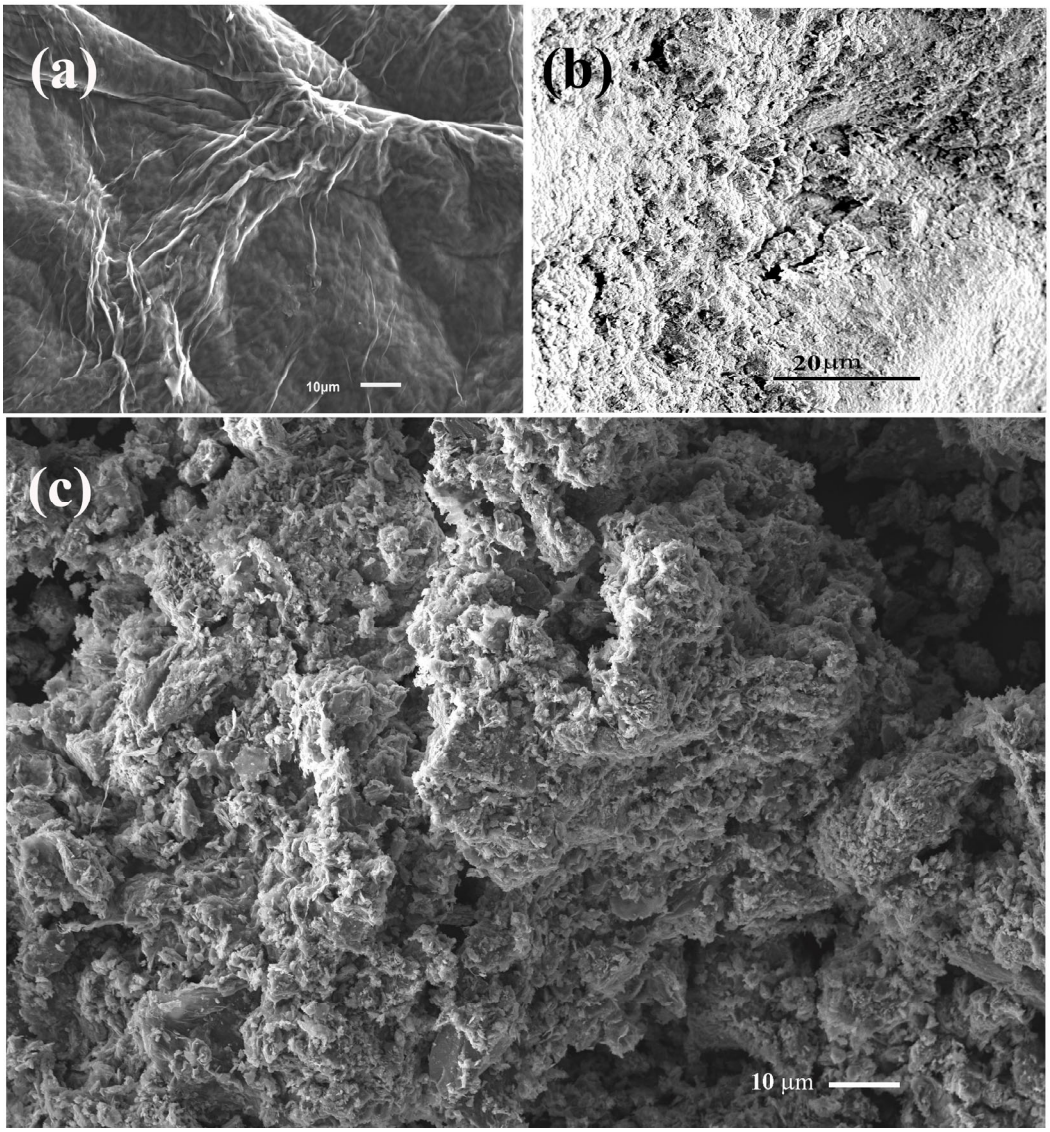


Figure 3. (**a**) Graphene oxide (GO) morphology; bar, 10 μm; (**b**) natural zeolite; bar, 20 μm; (**c**) nanocomposite of zeolite and graphene oxide, bar, 10 μm.

Figure 3b reveals the morphology of natural zeolite, where the presence of pores is evident at high magnification (bar, 20 μm). Zeolite exhibited a pellet-like morphology, with pellet dimensions ranging from 1.4 mm to 400 μm. The whitish color was attributed to its aluminosilicate composition. Additionally, some grains were measured, obtaining a size range between 69.51 μm and 1631.65 μm (Figure S1), in concordance with the technical specifications.

Figure 3c illustrates the ZGO nanocomposite with a GO concentration of 10 mg mL^{-1} at the same magnification as that of GO (bar, 10 μm). It is evident that the morphology underwent significant changes. Meanwhile, the wrinkled veils of GO remain visible, and zeolite can also be observed deposited onto the material. The 3D morphology of zeolite was altered due to the incorporation of the GO layers within the zeolitic domains. This is seen in several areas of the image that exhibit higher contrast and brightness—characteristic of heavier elements compared to carbon, such as aluminosilicates. Additionally, the characteristic whitish color shifted to a grayish tone, indicating ionic exchange due to the interaction with GO.

3.1.4. EDS Characterizations

Figure 4a shows the EDS spectrum of GO, which mainly revealed carbon (51.46%) and oxygen in GO composition (46.51%), confirming the added functional groups in graphite basal plane, forming GO. Despite the high percentages of these elements due to the presence of functional groups, we observed a small sulfur contribution (2.03%), likely originating from the synthesis process of graphene oxide [31]. In Figure 4b, the EDS spectrum of natural zeolite reveals that its chemical composition consisted mainly of oxygen (66.56%), silicon (23.64%), and aluminum (6.16%), with lower proportions of sodium (0.67%), potassium (1.46%), and calcium (1.51%). On the other hand, in Figure 4c, the EDS spectrum of the ZGO nanocomposite indicates that it was composed of oxygen (53.76%), carbon (20.90%), silicon (18.17%), aluminum (4.41%), sulfur (1.03%), potassium (1.06%), and calcium (0.69%). The presence of carbon within the nanocomposite structure suggests a redistribution of the percentage concentrations of elements such as silicon and aluminum, indicating an adjustment in the material's composition.

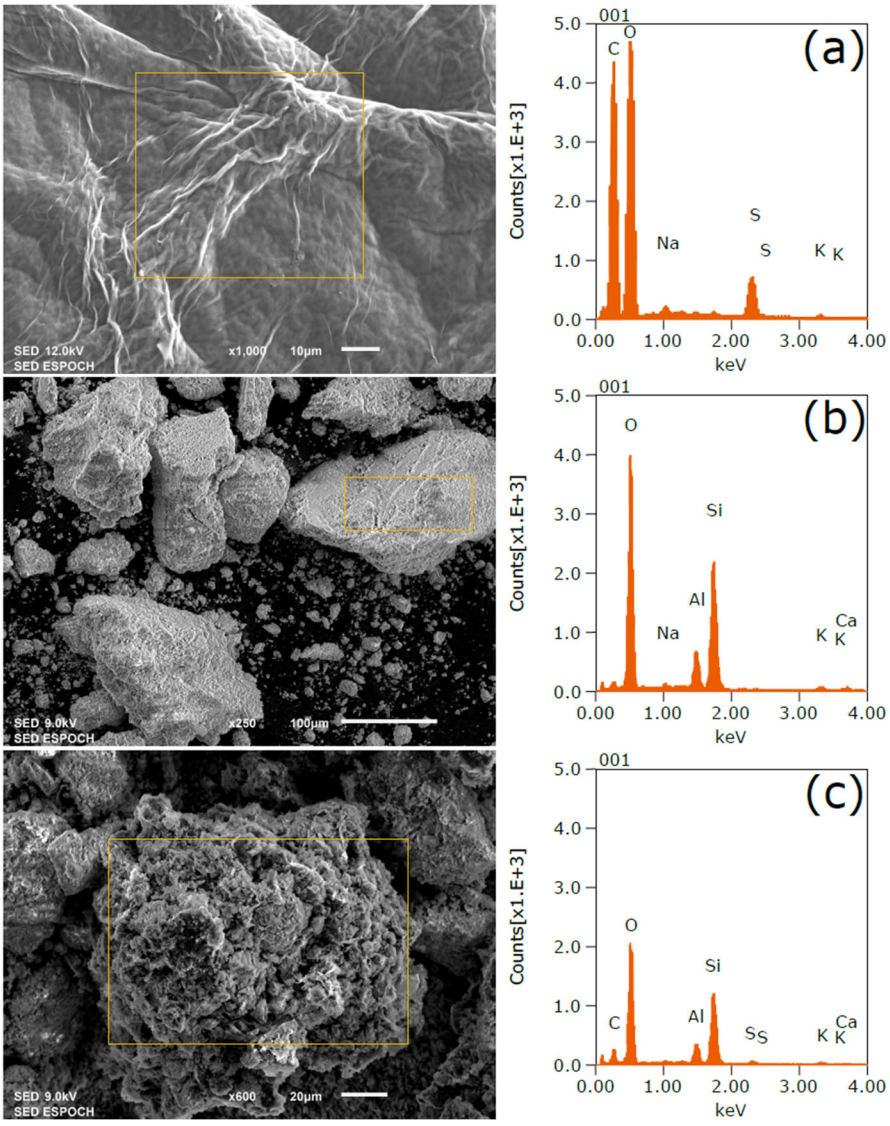


Figure 4. (**a**) Electron-dispersive spectroscopy (EDS) spectrum of graphene oxide; (**b**) EDS spectrum of natural zeolite (bar, 100 µm) (**c**) EDS spectrum of nanocomposite formed of natural zeolite and graphene oxide (ZOG).

The determination of surface area and pore size distribution was performed using the Brunauer–Emmett–Teller (BET) technique with an ASAP 2020 Plus system (Micromeritics Instrument Corp., Norcross, GA, USA) and liquid nitrogen (77 K). Figure S2a demonstrates an increase in the specific surface area of the ZGO material (1020 m^2 g^{-1}), which was attributed to the incorporation of graphene oxide (GO). The pore size distribution analysis revealed a heterogeneous structure, characterized by a higher proportion of mesopores (1.7–60 nm) and the presence of macropores (>60 nm, Figure S2b). This heterogeneity was likely due to the homogeneous dispersion of GO within the zeolitic matrix

3.2. Effects of Various Parameters on MB Removal

3.2.1. pH Influence

The determination of the point of zero charge (pH_{PZC}) is crucial for assessing the adsorption capacity of a material. In the case of zeolite (ZGO10), a calculated pH_{PZC} of 4.60 (Figure 5a) indicated that at a pH above this value, the material would acquire a net negative surface charge. This is attributed to the deprotonation of surface functional groups, such as carboxyl, epoxide, and hydroxyl groups, resulting in the generation of negatively charged sites. Consequently, the material exhibited enhanced adsorption capacity for methylene blue (MB), a cationic dye, due to strong electrostatic interactions. The pK of MB is 3.8, implying that at pH values greater than 3.8, the dye predominantly exists in its deprotonated, cationic form [45]. The electrostatic attraction between the negatively charged zeolite surface and the positively charged MB molecules will maximize the adsorption efficiency.

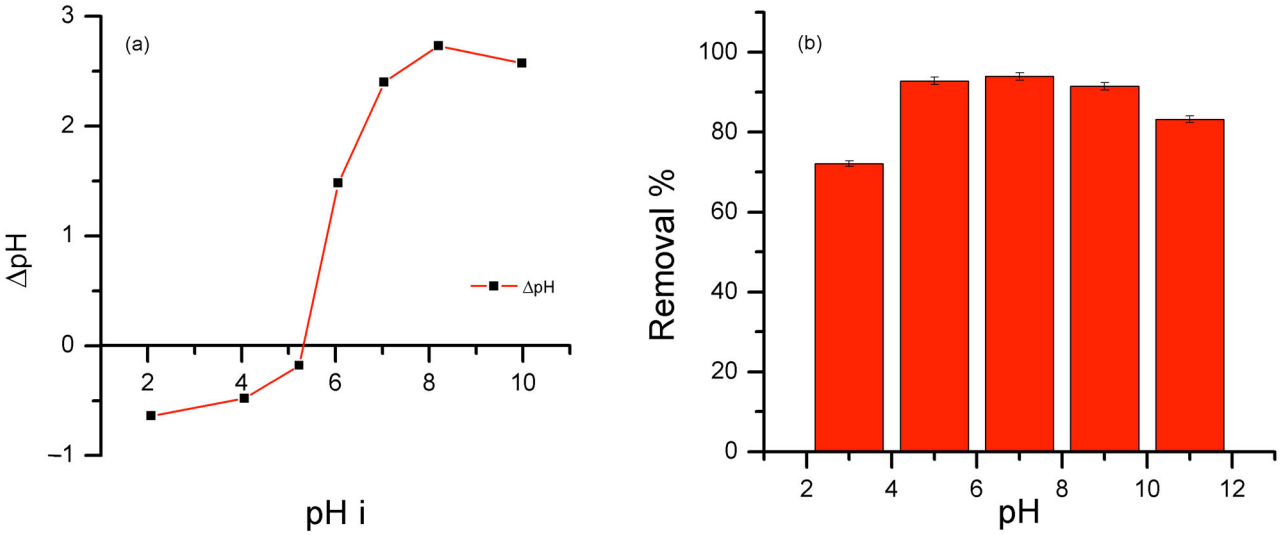


Figure 5. (**a**) Point of zero charge of ZGO10; (**b**) effect of pH on the equilibrium adsorption capacity of the composite ZGO10 towards MB.

Figure 5b illustrates the pH dependency of methylene blue (MB) adsorption onto ZGO. The adsorption capacity showed a significant increase within the pH range of 5 to 9, reaching a maximum efficiency of approximately 92%. This trend is primarily attributed to the electrostatic interactions between the negatively charged ZOG surface (pH_{PZC} = 5.3) and the cationic MB species (pKa = 3.8).

At pH values below 5, electrostatic repulsion and ionic competition reduced the adsorption efficiency, resulting in a lower removal rate of 73%. Conversely, at pH values above 10, the formation of complexes between hydroxide ions and MB molecules decreased the availability of the dye for adsorption. Based on these observations, a working pH of 6.0 was chosen to optimize MB adsorption.

3.2.2. Effect of Contact Time

In this study, the optimal contact time for the removal of the methylene blue (MB) dye using the ZGO2.5, ZGO5, and ZGO10 nanocomposites was determined. The efficiency of these composites was compared to that of their individual components graphene oxide and zeolite. To achieve this, the decrease in MB concentration (100 mg L^{-1}) was monitored as a function of the contact time.

A significant reduction in the concentration of methylene blue (Ce) was observed upon contact with graphene oxide (GO). This decrease occurred mainly during the first 30 min, reaching equilibrium at around 50 min (Figure 6a). The adsorption capacity of GO (qt) approached 90 mg g^{-1} (Figure 6b).

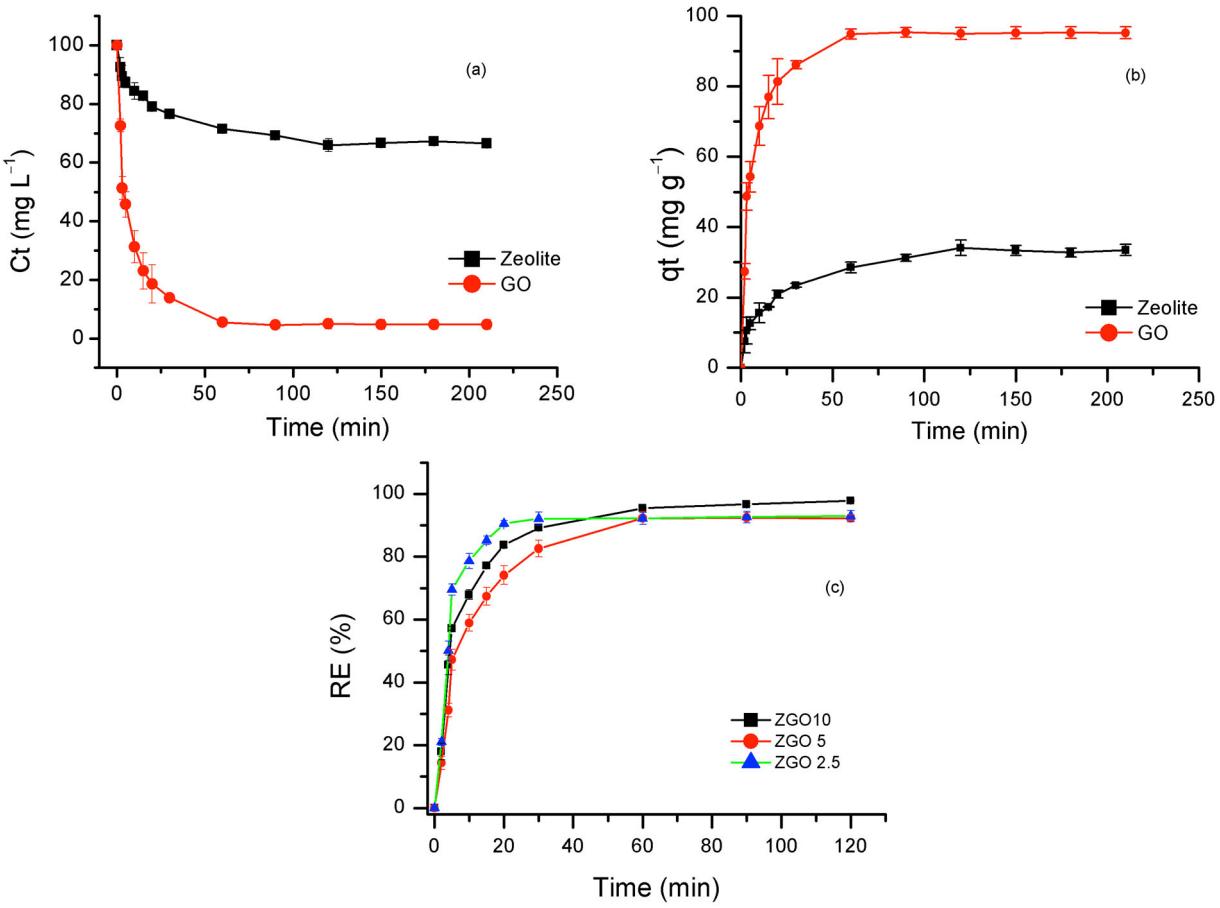


Figure 6. Contact time dependence of (**a**) MB concentration (Ct) and (**b**) adsorption capacity (qt) for pristine zeolite and GO; (**c**) MB removal efficiency (RE%) vs. contact time for the composite adsorbents.

In contrast, pristine zeolite allowed for a slower and less efficient reduction in Ct during the first 60 min. The minimum methylene blue concentration in the solution was reached at approximately 120 min, with an adsorption capacity of qt = 37 mg g^{-1}.

The difference in adsorption efficiency between GO and pristine zeolite is attributed to their distinct porous structures and physicochemical properties. Due to its laminar structure and high specific surface area [46], GO exhibits a superior adsorption capacity compared to pristine zeolite.

The compounds ZGO2.5, ZGO5, and ZGO10 exhibited adsorption kinetics intermediate between those of pristine zeolite and GO, reaching equilibrium in approximately 70 min. In all three cases, dye removal was close to 90%. The enhanced adsorption capacity compared to that of pristine zeolite suggests a synergy between GO and zeolite in these

compounds. This synergy could be attributed to a greater availability of active sites and a possible cooperative interaction between the two materials, facilitating faster and more efficient dye adsorption.

3.3. Adsorption Kinetics Studies

The experimental data were fitted to the pseudo-first-order, pseudo-second-order, and Elovich kinetic models to describe the adsorption kinetics of the materials.

The pseudo-first-order kinetic model assumes that the rate of adsorption is directly proportional to the number of active adsorption sites on the adsorbent surface. This model can be mathematically expressed as follows [38]:

$$\frac{dq_t}{dt} = k_1(q_e - q_t) \quad (3)$$

$$\log(q_e - q_t) = \log q_e - \frac{k_1}{2.303}t \quad (4)$$

where k_1 is the rate constant of the pseudo-first-order sorption process (min^{-1}), qt is the adsorption capacity at a specific time (t), and qe represents the equilibrium adsorption capacity (mg g^{-1}).

The pseudo-second-order kinetic model assumes that the rate of adsorption is proportional to the square of the number of unoccupied active sites. This model is described by the Ho equation [47]:

$$\frac{dq_t}{dt} = k_2(q_e - q_t)^2 \quad (5)$$

$$\frac{t}{qt} = \frac{1}{k_2 q_e^2} + \frac{1}{q_e}t \quad (6)$$

where qe and qt are the concentrations of MB per unit mass at equilibrium and time (t), respectively.

The Elovich model describes the heterogeneous adsorption of an analyte by chemisorption, assuming no interactions between the adsorbed species. It is expressed by the following equation [48]:

$$q_t = \left(\frac{1}{\beta}\right)\ln(\alpha\beta t + 1) \quad (7)$$

where α is the initial adsorption rate (mg.g^{-1}·min^{-1}), and β is a constant (mg g^{-1}) depending on the number of sites available for adsorption and desorption, related to surface coverage and activation energy.

The kinetic analysis presented in the Figure 7 illustrates the fit of the pseudo-first-order and pseudo-second-order models, both achieving a coefficient of determination (R^2) greater than 0.9, indicating their potential suitability. However, the pseudo-first-order model required longer contact times to reach equilibrium (plateau) compared to the pseudo-second-order model. Consequently, the pseudo-second-order model exhibited a better fit and aligned more closely with the data. In contrast, the Elovich model demonstrated a significantly poorer fit, as indicated by its low R^2 value, and was therefore excluded from further consideration. A comparison of the pseudo-first-order and pseudo-second-order models, based on the sum of squared errors (SSE) criterion, revealed that the pseudo-second-order model provided a more precise representation of the data.

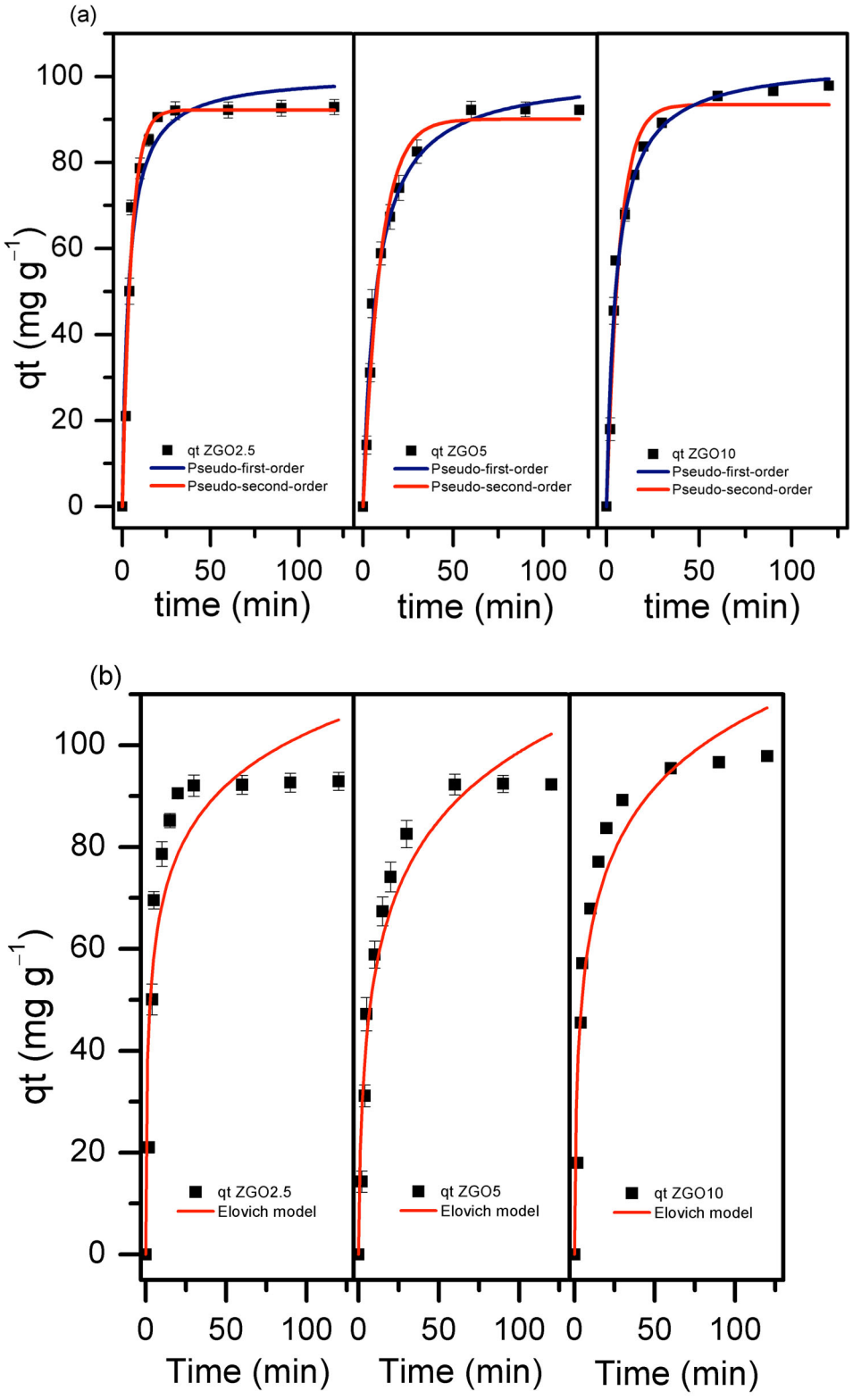


Figure 7. Adsorption kinetics of MB on ZGO2.5, ZGO5, and ZGO10 as a function of contact time (up to 120 min). (**a**) Pseudo-first- and -second order models; (**b**) Elovich model.

Graphene oxide, due to its large surface area, significantly enhanced the adsorption capacity of zeolite for methylene blue ions. This effect was attributed to π-π interactions between the aromatic ring of the dye and the graphene oxide structure [49], as well as to hydrogen bonding between the ammonium groups of methylene blue and the carboxylic

groups present in graphene oxide. This synergy greatly enhanced the adsorption capacity of the composite material.

As shown in Table 1, the theoretical (qtcal) and experimental (qtexp) values of the maximum adsorption capacity aligned closely. However, increasing the proportion of graphene oxide did not lead to a proportional enhancement in the composite material's adsorption capacity. This observation suggests that, while graphene oxide contributed additional active sites, its integration into the zeolite structure was limited, thereby restricting the full realization of its adsorption potential.

Table 1. Kinetic parameters of the pseudo-first-order model, the pseudo-second-order model, and the Elovich kinetic model.

	Adsorbents		
Parameters	**ZGO2.5**	**ZGO5.0**	**ZGO10**
Pseudo-first-order model			
$q_{e(exp)}$ (mg g^{-1})	90.92	91.28	97.95
$q_{e(cal)}$ (mg g^{-1})	92 ± 2	90 ± 2	93 ± 2
k_1 (min^{-1})	0.21 ± 0.020	0.105 ± 0.009	0.14 ± 0.01
R^2	0.9764	0.9805	0.9755
SSE	221	185	241
Pseudo-second-order model			
$q_{e(cal)}$ (mg g^{-1})	101 ± 4	101 ± 2	104 ± 3
k_2 (g mg^{-1} min^{-1})	0.0028 ± 0.0006	0.0013 ± 0.0002	0.0018 ± 0.0004
R^2	0.9503	0.9864	0.9833
SSE	169	129	164
Elovich model			
a (mg g^{-1} min^{-1})	153 ± 80	29 ± 6	58 ± 10
b (g mg^{-1})	0.068	0.052	0.055
R^2	0.8536	0.9457	0.9313
SSE	152	57	75

These findings validated the proposed model and suggested that the adsorption mechanism was based on a chemisorption process, involving significant chemical interactions between the adsorbate and the active sites of the material.

Intraparticle Diffusion Study

To elucidate the adsorption and mass transfer mechanisms of the dye onto ZGO, the Weber–Morris intraparticle diffusion (IPD) model was applied. The results revealed that the adsorption process involved multiple diffusion stages at varying rates, as reflected in the distinct linear regions of the plot. Each of these regions can be described by the following equation [38,50]:

$$qt = k_p t^{1/2} + C \quad (8)$$

where kp is the intraparticle diffusion (IPD) rate constant, and C represents the intercept at qt = 0, which is a constant related to the process. Thus, the linearized plot of qt (mg g^{-1}) as a function of $t^{1/2}$ ($min^{1/2}$) provides key insights into the different stages of the adsorption mechanism.

The contribution of the first diffusion step could be evaluated using the characteristic ratio, known as the initial adsorption ratio (Ri), defined by the following equation:

$$R_i = \frac{q_{ref} + C}{q_{ref}} \quad (9)$$

where qref is the adsorption capacity at the longest time, and C can be related to the boundary layer thickness. The parameters of the IPD model are summarized in Table 2.

Table 2. Parameters of the intraparticle diffusion (IPD) model for MB adsorption on ZGO2.5, ZGO5, and ZGO10.

Adsorbents	Kp (mg g^{-1} $min^{-1/2}$)	C (mg g^{-1})	Ri	R^2
ZGO2.5	29 ± 3	1.2 ± 0.6	0.98	0.9287
ZGO5.0	17 ± 1	6.2 ± 1.3	0.93	0.9888
ZGO10	22 ± 2	5.5 ± 1.5	0.92	0.9006

The diffusion of MB onto the three different composite materials, as observed in Figure 8, was concentrated in the initial stage (i), characterized by a high adsorption rate within the first minutes. This was attributed to the diffusion of the dye towards the external surface of ZGO and its subsequent fixation on the surface active sites. Subsequently, a second linear region (ii) was observed, indicating an intraparticle diffusion process, where the dye penetrated into the pores of the adsorbent following a concentration gradient. The final stage (iii), corresponding to the equilibrium region, was characterized by a very slow diffusion rate, probably due to the filling of the micropores and interactions between the adsorbed molecules. The value of the initial adsorption factor in the three materials fell within the range of 1 > Ri > 0.9, indicating weakly initial adsorption [50].

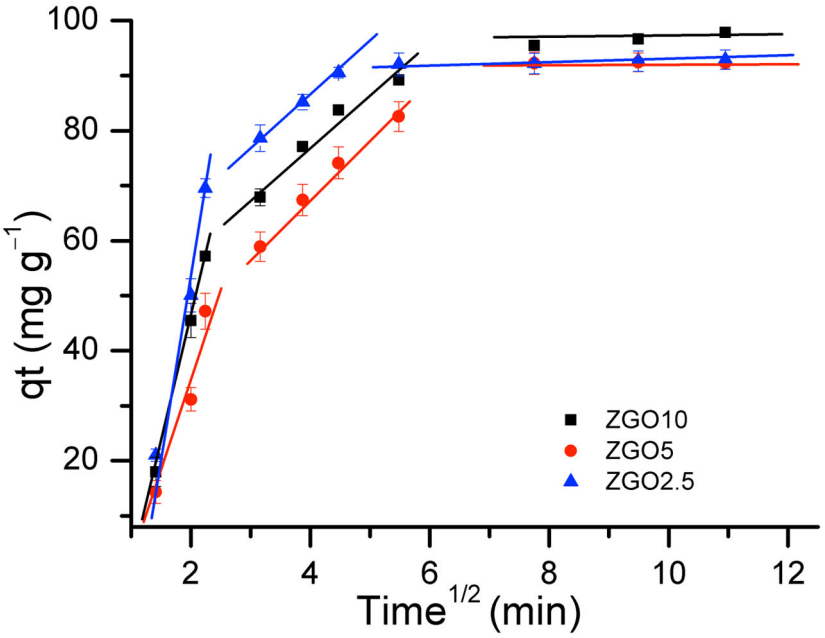


Figure 8. Intraparticle diffusion plot showing three regions of linearity (C_0 = 100 mg L^{-1}, T = 298 K).

3.4. Adsorption Isotherm

To describe the adsorption process in the composite materials at four different temperatures (298, 318, 323, and 333 K), the experimental data were fitted to the Langmuir, Freundlich, Temkin II and Dubinin–Radushkevich models. The Langmuir model assumes that adsorption occurs in a single molecular layer on a uniform surface, where the adsorption sites are energetically equivalent, and the adsorbed molecules do not interact with each other. The maximum adsorption capacity, representing the maximum amount of adsorbate that can be retained by the adsorbent per unit mass, is determined through the Langmuir equation [38,51].

$$q_e = \frac{q_m K_L C_e}{1 + K_L C_e} \quad (10)$$

where qm (mg g^{-1}) represents the maximum adsorption capacity, and K_L (L mg^{-1}) is the Langmuir constant, which is related to the adsorption free energy.

The Freundlich model assumes that adsorption occurs on a surface with a heterogeneous distribution of energy at the active sites. This implies that the adsorption capacity varies across different regions of the surface. This model is described by equation [5]

$$\log q_e = K_F C_e^{1/n} \quad (11)$$

where K_F is the adsorption capacity (mg L^{-1}), and n is the surface heterogeneity and intensity of adsorption.

The Temkin II model studies the linear decrease in the heat of adsorption as the surface coverage increases in an adsorption process, considering the interactions between the adsorbed molecules; this model is represented by the following equation [52,53]:

$$q_e = q_T \, ln(1 + K_T C_e) \quad (12)$$

where qT = qm/f, with f being a dimensionless constant given by the sum of the exponential factors of the adsorption and desorption first-order rate equations, and K_T their ratio [53,54].

The Dubinin–Radushkevich (D-R) model, a temperature-dependent model, is used to describe the adsorption mechanism, whether chemisorption or physisorption, on heterogeneous surfaces. It is based on the assumption of a Gaussian energy distribution [55]. The Dubinin–Radushkevich isotherm is represented by Equation (13) [54]

$$q_e = q_m e^{-\beta [RTln(\frac{Cs}{Ce})]^2} \quad (13)$$

where β is a constant related to the mean free energy of adsorption E = $1/\sqrt{2\beta}$, Cs is the solute solubility, R is the universal gas constant (8.314 J $mol^{-1} \cdot K^{-1}$), and T is the absolute temperature.

Methylene blue adsorption isotherms onto ZGO10 at several temperatures are reported in Figure 9.

The experimental data showed an increase in adsorption capacity with the temperature, clearly indicating that the adsorption process was endothermic. Therefore, a high and positive entropy change was expected to occur, driving the adsorption process.

For the fitted models, it was observed that the determination coefficients (R^2) were greater than 0.94 in all cases, except at 298 K, where the values were below 0.92.

However, the Langmuir model described the experimental data the worst. This was to be expected due to the inherently heterogeneous nature of the composite material used as an adsorbent. In fact, all the other isotherm models accounted for a certain heterogeneity of the adsorbent surface, with different binding sites belonging to the zeolitic fraction and the GO graphite fraction. The fitted parameters for each isotherm model are reported in Table 3. The estimated maximum adsorption capacity using the Langmuir model was around 58 mg g^{-1} at room temperature and up to 83 mg g^{-1} at 323 K. In the Freundlich model, the non-linear power parameter "n" assumed a mean value of 0.28 ± 0.06 (Table 3), which remained consistent across the tested temperatures and within the standard deviation, indicating goodness of fit.

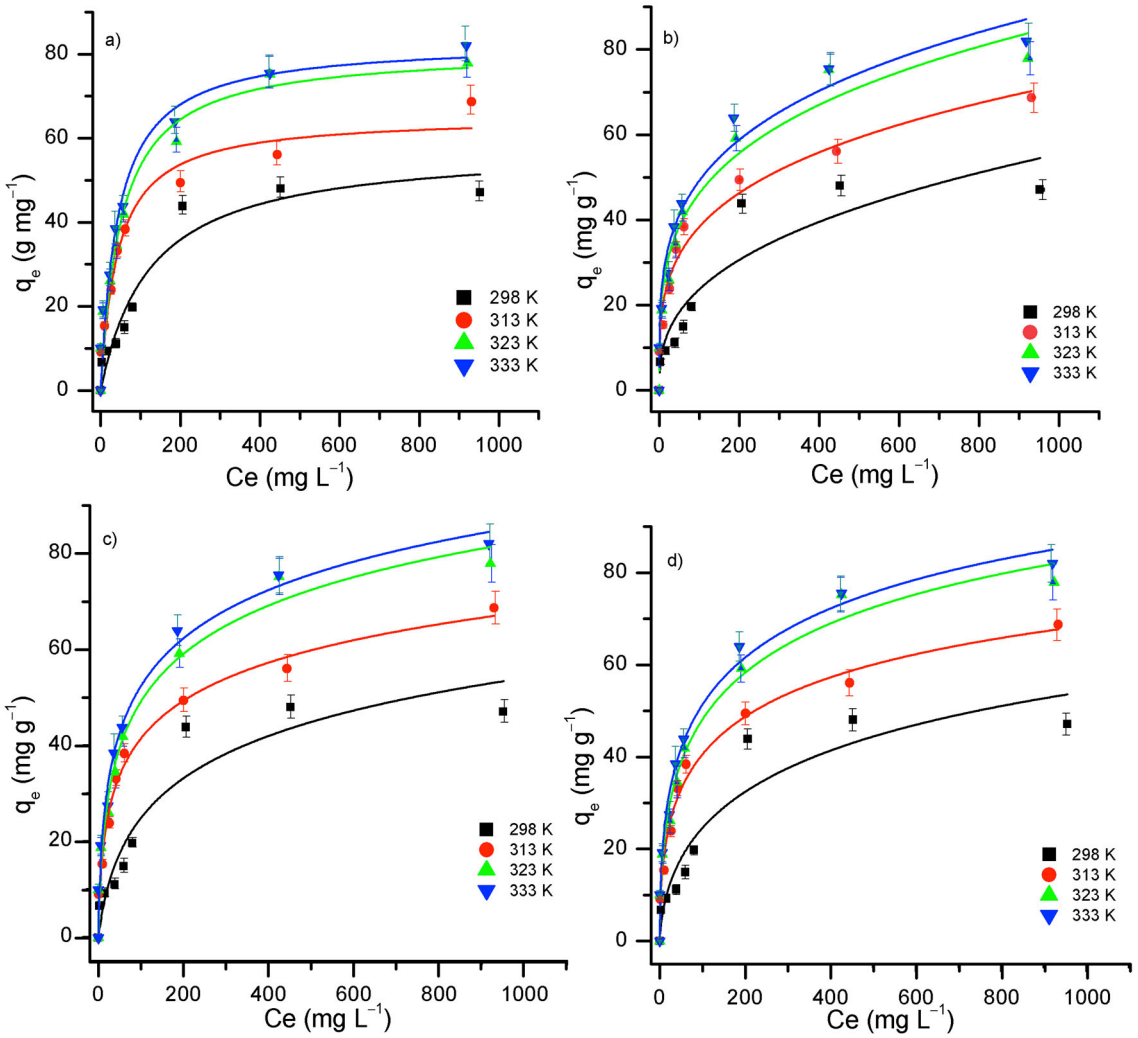


Figure 9. Fitting of the experimental isotherm data at different temperatures using the isotherm models of (**a**) Langmuir; (**b**) Freundlich; (**c**) Temkin; (**d**) Dubinin–Radushkevich.

The Temkin model also fitted the experimental data well and supported the idea of a non-uniform surface. This model assumes a distribution of adsorption energies on the adsorbent and considers that the adsorbed molecules interact with one another, affecting the adsorption energy of subsequent molecules [54,55].

The Dubinin–Radushkevich (D-R) model provided additional insights into the adsorption mechanism. This model showed an adequate fit (R^2) at temperatures above 298 K, suggesting that the adsorption process occurred in pores and was dominated by energy heterogeneity and diffusion. This behavior was supported by the intraparticle diffusion analysis of Weber–Morris, where the final stage corresponded to diffusion within the pores. The maximum adsorption capacity (qm) estimated by the D-R model ranged from 84 to 119 mg g^{-1}, exceeding the values determined by the Langmuir model. Considering the nature of the process, the β parameter from the D-R model allowed for the calculation of the mean free energy ($E = 1/\sqrt{2\beta}$), with values in the range of 9.4 to 13.0 kJ mol^{-1}. These results suggested a chemisorption mechanism [56]. As the temperature increased, the adsorbate molecules acquired greater kinetic energy, increasing their mobility, which facilitated their dispersion into the pores and enhanced their fixation at the active sites of the adsorbent.

Table 3. Parameters of the Langmuir, Freundlich, Temkin and D-R isotherm adsorption models, considering different temperatures.

Isotherm Parameters	Temperatures			
	298 K	**318 K**	**323 K**	**333 K**
Langmuir model				
KL (L mg^{-1})	0.0085 ± 0.001	0.023 ± 0.005	0.020 ± 0.005	0.023 ± 0.005
qm (mg g^{-1})	58 ± 6	65 ± 4	81 ± 5	83 ± 5
R^2	0.92371	0.9433	0.9401	0.9487
SSE	149	143	233	215
Freundlich model				
K_F ($mg^{(1-n)}g^{-1}$ $L^{1/n}$)	4.3 ± 1.9	11.3 ± 1.4	13.5 ± 2.3	15.1 ± 2.2
n	0.37 ± 0.07	0.27 ± 0.02	0.26 ± 0.02	0.25 ± 0.03
R^2	0.8310	0.9686	0.9545	0.9620
SSE	329	79	177	159
Temkin II model				
q_T (mg g^{-1})	14 ± 3	12 ± 1	15 ± 2	14 ± 1
K_T (L mg^{-1})	0.053 ± 0.03	0.35 ± 0.11	0.28 ± 0.12	0.35 ± 0.14
R^2	0.9077	0.9828	0.9681	0.9754
SSE	229	62	172	144
Dubinin–Radushkevich model				
qm (mg g^{-1})	84 ± 14	95 ± 4	117 ± 9	119 ± 7
$\beta \times 10^{-9}$ (mol^2 j^{-2})	5.68 ± 1.01	3.41 ± 0.22	3.34 ± 0.33	2.98 ± 0.26
E (kj mol^{-1})	9.4 ± 1.7	12.1 ± 0.6	12.2 ± 0.9	13.0 ± 0.8
R^2	0.8998	0.9873	0.9714	0.9776
SSE	248	46	155	131

The adsorption mechanism of methylene blue (MB) onto ZGO can be explained through a synergistic process involving the following components: (1) electrostatic interactions; (2) π-π interactions; (3) hydrogen bonding; (4) cation exchange; (5) diffusion within the microporous structure (Figure 10). MB^+ is electrostatically attracted to the negatively charged sites of zeolite and the functional groups of GO. Simultaneously, π-π stacking interactions occur between the aromatic rings of MB and the graphenic regions of GO, stabilizing the adsorption. Additionally, the hydroxyl (-OH) and carboxyl ($-COO^-$) groups of GO form hydrogen bonds with MB, facilitating its immobilization. The ion exchange capacity of zeolite, involving the exchange of cations (e.g., Na^+, K^+, Ca^{2+}) with MB^+ from the solution, further enhances adsorption. Finally, MB can diffuse into the micropores of zeolite, where it becomes trapped through physical and chemical interactions, increasing the stability of the adsorption process. This combination of mechanisms grants ZGO a high capacity for removing cationic dyes from aqueous solutions.

The mechanism can be represented as follows:

(1) $ZGO^- + MB^+ \leftrightharpoons ZGO - MB$;
(2) $\pi - \pi$ interactions : $ZGO\cdot - \cdot - MB$;
(3) $ZGO - OH - - - MB$;
(4) $MB(solutions) \longrightarrow$ diffusion $\longrightarrow$ retention in ZGO micropores;
(5) $ZGO - Mn^+ + MB^+ \leftrightarrows ZGO - MB^+ + Mn^+$.

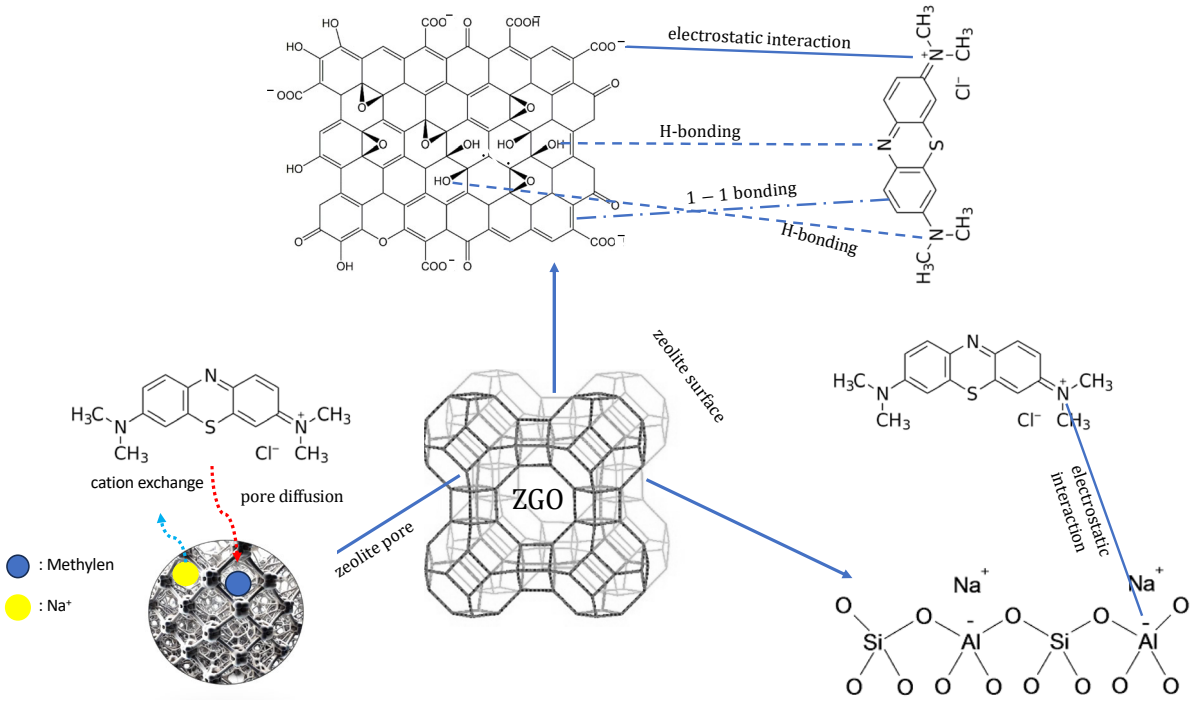


Figure 10. Illustrative diagram of the adsorption mechanisms of MB^+ onto ZGO including arrows identifying distinct material regions (surface and pores).

Mn^+ is an exchangeable cation present in zeolite (Na^+, K^+, Ca^{2+}).

It is important to highlight the significant increase in methylene blue (MB) adsorption when incorporating graphene oxide into the zeolite structure. The contact time analysis showed that pristine zeolite had an adsorption capacity of qt = 37 mg g^{-1} to 120 min, which increased with the addition of graphene oxide (Figure 6). This composite material achieved a maximum adsorption capacity (qm) of 119 mg g^{-1}, which is a competitive value compared to those of other adsorbents used in industrial applications (Table 4). Moreover, this performance underscored the feasibility of using zeolite, a low-cost material, as a base for developing advanced adsorbents. The combination with graphene oxide may not only enhance its efficiency but also expand its potential applications in various industrial processes, reinforcing its promise as an effective and economical adsorbent.

Table 4. Maximum adsorption capacities of ZGO10 in relation to other adsorbents.

Adsorbents	Adsorption Capacity (mg g^{-1})	References
Ag-Fe_3O_4–polydopamine	45	[57]
Magnetic carboxyl functional nanoporous polymer	58	[58]
Nanosheet–MFI zeolite (NZ)	476	[19]
NaA	65	[21]
Zeolite-A/reduced graphene oxide	667	[22]
Magnetic zeolite	10	[23]
Activated carbon	114	[59]
Citrus hystrix–rGO	276	[60]
Eco-friendly rGO	122	[5]
ASAC	37	[14]
ß-cyclodextrin/MGO	94	[51]
ZGO10	119	This work

3.5. Adsorption Thermodynamics

To analyze the energy variations associated with the adsorption of MB onto ZOG10 nanosheets, thermodynamic parameters such as the standard Gibbs free energy change (ΔG^0), enthalpy change (ΔH^0), and entropy change (ΔS^0) were calculated using Equation (14) and the van't Hoff Equation (15), which expresses the changes of the equilibrium constant with the temperature [61]

$$\Delta G^0 = -RT\ln K_e \tag{14}$$

$$\frac{d\ln K_e}{dT} = \frac{\Delta H^0}{RT^2} \tag{15}$$

For proper application of the van't Hoff equation, the equilibrium constant, Ke, must be dimensionless. Since Ke represents the thermodynamic equilibrium constant, it is derived from the distribution coefficient Kd of MB, related to MB distribution between the adsorbent and the aqueous phase (Figure S3). Using the linear portion of the adsorption isotherm data at four different temperatures, Kd (L mg^{-1}) is determined by fitting the data to Equation (16) [62]

$$q_e = K_d C_e \tag{16}$$

To obtain a dimensionless equilibrium constant suitable for the van't Hoff equation, the following conversion (Equation (17)) was employed:

$$K_e = \frac{K_d M_a * 1000}{\gamma_e} \tag{17}$$

where Ma represents the molar weight of MB (319.85 g mol^{-1}), and γe is the activity coefficient (dimensionless) of MB in solution [63], which, in the infinite dilution scale, approaches unity (γe = 1) [64]. Thus, the entropy (ΔS^0) and enthalpy (ΔH^0) parameters can be determined from Equation (17), which is a combination of Equations (14) and (15) [63,65], by fitting the data of $\ln K_e$ vs. T^{-1} and assuming that the standard enthalpy change is independent of T in the small temperature interval considered (Figure 11):

$$\ln\frac{K_e}{\gamma_e} = \frac{\Delta S^0}{R} - \frac{\Delta H^0}{RT} \cong \ln K_e \tag{18}$$

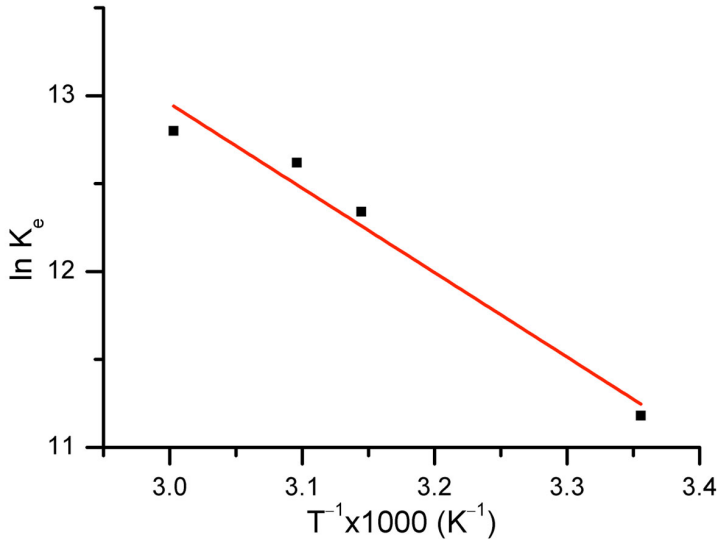


Figure 11. van't Hoff regression for determining the thermodynamic parameters of MB adsorption onto ZOG10.

The adsorption process is classified as physisorption when the ΔG° values range from 0 to −20 kJmol^{-1}, while ΔG° values between −80 and −400 kJmol^{-1} indicate a chemisorption process. However, the distinction between these two categories is not entirely precise [5]. The calculated ΔG° values, ranging from −29.1 to −35.5 kJmol^{-1}, indicated that the adsorption of MB onto ZGO10 occurred through a hybrid mechanism involving both physisorption and chemisorption. The spontaneity of this process at different temperatures, evidenced by the negative ΔG° values, suggested a strong interaction between the MB ions and the ZGO10 surface, which was driven by the relatively high entropy change associated to the adsorption process (Table 5). This could be due to an ion exchange mechanism between MB and the cations contained in the composite material.

Table 5. Thermodynamic parameters for MB adsorption on ZGO10.

T (K)	K_d (L mg^{-1})	ΔG^0 (kJ mol^{-1})	ΔH^0 (kJ mol^{-1})	ΔS^0 (J mol^{-1} K^{-1})
298	0.22 ± 0.02	−29.1 ± 0.2	40 ± 1	228 ± 6
318	0.78 ± 0.09	−32.6 ± 0.5		
323	0.95 ± 0.12	−33.9 ± 0.5		
333	1.14 ± 0.19	−35.5 ± 0.9		

On the other hand, the determined value of ΔH° provided insights into the adsorption mechanism. Enthalpy values between 2.1 and 20.9 kJmol^{-1} are characteristic of physical adsorption, dominated by low-energy interactions such as van der Waals forces, whereas values in the range of 80 to 200 kJ mol^{-1} are typical of chemisorption processes, involving stronger chemical bonds. Therefore, a ΔH° of 40 kJmol^{-1} suggested that the predominant mechanism was a physico-chemical adsorption process, where physical and weak chemical interactions coexist, in line with the previously discussed Gibbs free energy values [61,66].

3.6. Regeneration of ZGO Analysis

The regeneration and stability of zeolite with graphene oxide (ZGO) were evaluated through successive cycles of desorption and readsorption. Desorption was performed using 10 mL of 0.1 N HCl under agitation at 200 rpm for 4 h. Subsequently, the material was separated, washed, and dried before being subjected to readsorption in 10 mL of a methylene blue (MB) solution at 10 mg L^{-1}, with agitation at 250 rpm for 3 h. This procedure was repeated for five cycles.

The results indicated that, during the first three cycles, the adsorption capacity of ZGO remained nearly unchanged, with MB removal slightly decreasing from 98% to 96%. However, from the fourth cycle onward, a slow decline in efficiency was observed, reaching 84% in the fifth cycle (Figure S4). This trend suggested a gradual loss of adsorption capacity, possibly due to incomplete desorption, leading to residual MB accumulation within the zeolite pores, thereby reducing the accessibility of active sites and partially blocking the adsorption channels. Additionally, repeated exposure to the acidic medium could induce structural modifications in zeolite, such as cation leaching, and alter the functionalization of GO, ultimately impairing its long-term performance.

The obtained results demonstrate the remarkable stability and reusability of ZGO in multiple cycles of MB adsorption. The high removal efficiency observed, even after several cycles, suggests that ZGO exhibits excellent adsorption properties for MB and strong potential for application in wastewater treatment systems.

4. Conclusions

This study successfully improved the adsorption capacity of natural zeolite by forming a nanocomposite with graphene oxide. A simple thermal process was used to modify

the material's structure, resulting in the nanocomposites ZGO2.5, ZGO5, and ZGO10. Characterization techniques such as UV-Vis and FTIR spectroscopy, SEM, BET technique, and EDS confirmed the impregnation of graphene oxide onto zeolite. These analyses also revealed an increased surface area and enhanced stability, further supported by the presence of graphene oxide's characteristic functional groups. The significant increase in adsorption capacity is attributed to the presence of these functional groups and the π-π interactions between the aromatic ring of methylene blue (MB) and the structure of the zeolite–graphene oxide nanocomposite (ZGO). Adsorption experiments were conducted in a pH range of 5 to 10, observing that the adsorption capacity increased with temperature. A maximum adsorption capacity of 119 mg g^{-1} was achieved at 333 K. The adsorption mechanism was best described by the pseudo-second-order kinetic model, while the adsorption isotherms showed the best fit to the Freundlich and D-R models. The thermodynamic analysis revealed that the adsorption process was physico-chemical in nature, spontaneous, and endothermic. Thanks to the improved adsorption capacity provided by the combination of zeolite and graphene oxide, this composite material emerges as a low-cost and highly efficient alternative for the treatment and removal of dye contaminants in industrial wastewater. Additionally, the material demonstrated high reusability, maintaining its adsorption performance for up to five cycles, with minimal capacity loss.

Supplementary Materials: The following supporting information can be downloaded at https://www.mdpi.com/article/10.3390/app15052824/s1, Figure S1. Natural zeolite micrograph and measurements of grains. Figure S2. (a) BET surface area plot of ZGO10; (b) pore size distribution in ZGO10. Figure S3. Linear fit of adsorption isotherm data section. (a) 298 K; (b) 313 K; (c) 323 K; (d) 333 K. Figure S4. Reusability study of the solution containing 10 mg of ZG10 in 10 mL of MB solution (10 mg $mL^{-}1$), using 10 mL of 0.1 N HCl as the desorption liquid at 298 K for 3 h.

Author Contributions: G.T.-U.: conceptualization, methodology, writing—original draft preparation. C.C.: validation, investigation, formal analysis. S.P.: validation, formal analysis, investigation. A.B.: data curation, writing—review and editing. F.A.A.: conceptualization, data curation, writing—original draft preparation, investigation. All authors have read and agreed to the published version of the manuscript.

Funding: This research was funded by Tech4You—Technologies for Climate Change Adaptation and Quality of Life Improvement grant number [ECS 00000009, CUP H23C22000370006].

Institutional Review Board Statement: Not applicable.

Informed Consent Statement: Not applicable.

Data Availability Statement: The original contributions presented in this study are included in the article/Supplementary Material. Further inquiries can be directed to the corresponding author.

Acknowledgments: The authors are very thankful to the Faculty of Sciences—ESPOCH for the facilities provided for the UV-Vis and SEM characterization.

Conflicts of Interest: The authors declare no conflicts of interest.

References

1. Assembly, U.G. Resolution Adopted by the General Assembly on 25 September 2015. Transforming Our World: The 2030 Agenda for Sustainable Development. 2015. Available online: https://www.un.org/en/development/desa/population/migration/generalassembly/docs/globalcompact/A_RES_70_1_E.pdf (accessed on 8 January 2025).
2. Bailey, K.; Basu, A.; Sharma, S. The Environmental Impacts of Fast Fashion on Water Quality: A Systematic Review. *Water* **2022**, *14*, 1073. [CrossRef]
3. Al-Asadi, S.T.; Al-Qaim, F.F.; Al-Saedi, H.F.S.; Deyab, I.F.; Kamyab, H.; Chelliapan, S. Adsorption of methylene blue dye from aqueous solution using low-cost adsorbent: Kinetic, isotherm adsorption, and thermodynamic studies. *Environ. Monit. Assess.* **2023**, *195*, 676. [CrossRef] [PubMed]

4. Rahmi; Ismaturrahmi; Mustafa, I. Methylene blue removal from water using H_2SO_4 crosslinked magnetic chitosan nanocomposite beads. *Microchem. J.* **2019**, *144*, 397–402. [CrossRef]
5. Arias, F.A.; Guevara, M.; Tene, T.; Angamarca, P.; Molina, R.; Valarezo, A.; Salguero, O.; Gomez, C.V.; Arias, M.; Caputi, L.S. The Adsorption of Methylene Blue on Eco-Friendly Reduced Graphene Oxide. *Nanomaterials* **2020**, *10*, 681. [CrossRef] [PubMed]
6. Fito, J.; Abewaa, M.; Mengistu, A.; Angassa, K.; Ambaye, A.D.; Moyo, W.; Nkambule, T. Adsorption of methylene blue from textile industrial wastewater using activated carbon developed from Rumex abyssinicus plant. *Sci. Rep.* **2023**, *13*, 5427. [CrossRef] [PubMed]
7. Bhatia, D.; Sharma, N.R.; Singh, J.; Kanwar, R.S. Biological methods for textile dye removal from wastewater: A review. *Crit. Rev. Environ. Sci. Technol.* **2017**, *47*, 1836–1876. [CrossRef]
8. Li, D.; Hua, T.; Yuan, J.; Xu, F. Methylene blue adsorption from an aqueous solution by a magnetic graphene oxide/humic acid composite. *Colloids Surf. A Physicochem. Eng. Asp.* **2021**, *627*, 127171. [CrossRef]
9. Wang, C.; Wang, F.; Xu, M.; Zhu, C.; Fang, W.; Wei, Y. Electrocatalytic degradation of methylene blue on Co doped Ti/TiO2 nanotube/PbO2 anodes prepared by pulse electrodeposition. *J. Electroanal. Chem.* **2015**, *759*, 158–166. [CrossRef]
10. Patel, P.; Gupta, P.; Sujata, K.; Solanki, R.G. Photocatalytic Degradation of Methylene Blue Dye Using Copper Selenide Nanoparticles Prepared by Co- Precipitation Method. *J. Clust. Sci.* **2024**, *35*, 191–199. [CrossRef]
11. Jin, X.; Jiang, M.Q.; Shan, X.Q.; Pei, Z.G.; Chen, Z. Adsorption of methylene blue and orange II onto unmodified and surfactant-modified zeolite. *J. Colloid Interface Sci.* **2008**, *328*, 243–247. [CrossRef]
12. Calimli, M.H.; Nas, M.S.; Burhan, H.; Mustafov, S.D.; Demirbas, Ö.; Sen, F. Preparation, characterization and adsorption kinetics of methylene blue dye in reduced-graphene oxide supported nanoadsorbents. *J. Mol. Liq.* **2020**, *309*, 113171. [CrossRef]
13. Zhang, W.; Yan, H.; Li, H.; Jiang, Z.; Dong, L.; Kan, X.; Yang, H.; Li, A.; Cheng, R. Removal of dyes from aqueous solutions by straw based adsorbents: Batch and column studies. *Chem. Eng. J.* **2011**, *168*, 1120–1127. [CrossRef]
14. Djilani, C.; Zaghdoudi, R.; Djazi, F.; Bouchekima, B.; Lallam, A.; Modarressi, A.; Rogalski, M. Adsorption of dyes on activated carbon prepared from apricot stones and commercial activated carbon. *J. Taiwan Inst. Chem. Eng.* **2015**, *53*, 112–121. [CrossRef]
15. Rahman, M.S. Adsorption of Methyl Blue onto Activated Carbon Derived from Red Oak (Quercus rubra) Acorns: A 26 Factorial Design and Analysis. *Water Air Soil. Pollut.* **2021**, *232*, 1. [CrossRef]
16. Jawad, H.; Rashid, R.A.; Ishak, M.A.M.; Wilson, L.D. Adsorption of methylene blue onto activated carbon developed from biomass waste by H2SO4 activation: Kinetic, equilibrium and thermodynamic studies. *Desalination Water Treat.* **2016**, *57*, 25194–25206. [CrossRef]
17. Aichour, A.; Zaghouane-Boudiaf, H.; Iborra, C.V.; Polo, M.S. Bioadsorbent beads prepared from activated biomass/alginate for enhanced removal of cationic dye from water medium: Kinetics, equilibrium and thermodynamic studies. *J. Mol. Liq.* **2018**, *256*, 533–540. [CrossRef]
18. Wang, S.; Peng, Y. Natural zeolites as effective adsorbents in water and wastewater treatment. *Chem. Eng. J.* **2010**, *156*, 11–24. [CrossRef]
19. Wang, S.; Peng, Y. Efficient and fast adsorption of methylene blue dye onto a nanosheet MFI zeolite. *J. Solid. State Chem.* **2021**, *295*, 121917. [CrossRef]
20. Zhou, Y.; Lu, J.; Zhou, Y.; Liu, Y. Recent advances for dyes removal using novel adsorbents: A review. *Environ. Pollut.* **2019**, *252*, 352–365. [CrossRef]
21. Sapawe, N.; Jalil, A.; Triwahyono, S.; Shah, M.; Jusoh, R.; Salleh, N.; Hameed, B.; Karim, A. Cost-effective microwave rapid synthesis of zeolite NaA for removal of methylene blue. *Chem. Eng. J.* **2013**, *229*, 388–398. [CrossRef]
22. Farghali, M.A.; Abo-Aly, M.M.; Salaheldin, T.A. Modified mesoporous zeolite-A/reduced graphene oxide nanocomposite for dual removal of methylene blue and Pb^{2+} ions from wastewater. *Inorg. Chem. Commun.* **2021**, *126*, 108487. [CrossRef]
23. Wang, C.; Yu, J.; Feng, K.; Wang, L.; Huang, J. Synthesis of porous magnetic zeolite-based material and its performance on removal of Cd2+ ion and methylene blue from aqueous solution. *Microporous Mesoporous Mater.* **2022**, *345*, 112256. [CrossRef]
24. Bogdanov, B.; Georgiev, D.; Angelova, K.; Yaneva, K. Economics and Society development on the Base of Knowledge. In Proceedings of the International Science Conference, Stara Zagora, Bulgaria, 4–5 June 2009; Volume VII, pp. 1–5.
25. Akyalcin, S.; Akyalcin, L.; Ertugrul, E. Modification of natural clinoptilolite zeolite to enhance its hydrogen adsorption capacity. *Res. Chem. Intermed.* **2024**, *50*, 1455–1473. [CrossRef]
26. Wang, C.; Yu, J.; Feng, K.; Guo, H.; Wang, L. Alkali treatment to transform natural clinoptilolite into zeolite Na–P: Influence of NaOH concentration. *J. Phys. Chem. Solids* **2022**, *168*, 110827. [CrossRef]
27. Peng, W.; Li, H.; Liu, Y.; Song, S. Adsorption of methylene blue on graphene oxide prepared from amorphous graphite: Effects of pH and foreign ions. *J. Mol. Liq.* **2016**, *221*, 82–87. [CrossRef]
28. Hummers, W.S.; Offeman, R.E. Preparation of Graphitic Oxide. *J. Am. Chem. Soc.* **1958**, *80*, 1339. [CrossRef]
29. Marcano, D.C.; Kosynkin, D.V.; Berlin, J.M.; Sinitskii, A.; Sun, Z.; Slesarev, A.; Alemany, L.B.; Lu, W.; Tour, J.M. Improved Synthesis of Graphene Oxide. *ACS Nano* **2010**, *4*, 4806–4814. [CrossRef]

30. Yan, J.A.; Chou, M.Y. Oxidation functional groups on graphene: Structural and electronic properties. *Phys. Rev. B Condens. Matter Mater. Phys.* **2010**, *82*, 21–24. [CrossRef]
31. Tene, T.; Usca, G.T.; Guevara, M.; Molina, R.; Veltri, F.; Arias, M.; Caputi, L.S.; Gomez, C.V. Toward large-scale production of oxidized graphene. *Nanomaterials* **2020**, *10*, 279. [CrossRef]
32. Dhar, L.; Hossain, S.; Rahman, S.; Quraishi, S.B.; Saha, K.; Rahman, F.; Rahman, M.T. Adsorption Mechanism of Methylene Blue by Graphene Oxide-Shielded Mg–Al-Layered Double Hydroxide From Synthetic Wastewater. *J. Phys. Chem. A* **2021**, *125*, 954–965. [CrossRef]
33. Hussein, M.Z. Adsorption of Methylene Blue onto Treated Activated Carbon. 2007. Available online: https://www.researchgate.net/publication/251289860 (accessed on 18 December 2024).
34. Mani, S.K.; Bhandari, R. Microwave-assisted synthesis of self-assembled network of Graphene oxide-Polyethylenimine-Polyvinyl alcohol hydrogel beads for removal of cationic and anionic dyes from wastewater. *J. Mol. Liq.* **2022**, *345*, 117809. [CrossRef]
35. Abdi, G.; Alizadeh, A.; Amirian, J.; Rezaei, S.; Sharma, G. Polyamine-modified magnetic graphene oxide surface: Feasible adsorbent for removal of dyes. *J. Mol. Liq.* **2019**, *289*, 111118. [CrossRef]
36. Lopez-Ramon, M.V.; Stoeckli, F.; Moreno-Castilla, C.; Carrasco-Marin, F. On the characterization of acidic and basic surface sites on carbons by various techniques. *Carbon* **1999**, *37*, 1215–1221. [CrossRef]
37. Riva, L.; Pastori, N.; Panozzo, A.; Antonelli, M.; Punta, C. Nanostructured cellulose-based sorbent materials for water decontamination from organic dyes. *Nanomaterials* **2020**, *10*, 1570. [CrossRef]
38. Arias, E.A.; Beneduci, A.; Chidichimo, F.; Furia, E.; Straface, S. Study of the adsorption of mercury (II) on lignocellulosic materials under static and dynamic conditions. *Chemosphere* **2017**, *180*, 11–23. [CrossRef]
39. Concepción-Rosabal, B.; Rodríguez-Fuentes, G.; Bogdanchikova, N.; Bosch, P.; Avalos, M.; Lara, V.H. Comparative study of natural and synthetic clinoptilolites containing silver in different states. *Microporous Mesoporous Mater.* **2005**, *86*, 249–255. [CrossRef]
40. Eda, G.; Ball, J.; Mattevi, C.; Acik, M.; Artiglia, L.; Granozzi, G.; Chabal, Y.; Anthopoulos, T.D.; Chhowalla, M. Partially oxidized graphene as a precursor to graphene. *J. Mater. Chem.* **2011**, *21*, 11217–11223. [CrossRef]
41. Acik, M.; Lee, G.; Mattevi, C.; Pirkle, A.; Wallace, R.M.; Chhowalla, M.; Cho, K.; Chabal, Y. The role of oxygen during thermal reduction of graphene oxide studied by infrared absorption spectroscopy. *J. Phys. Chem. C* **2011**, *115*, 19761–19781. [CrossRef]
42. Hontoria-Lucas, C.; López-Peinado, A.J.; López-González, J.D.D.; Rojas-Cervantes, M.L.; Martín-Aranda, R.M. Study of Oxygen-Containing Groups in a Series of Graphite Oxides: Physical and Chemical. *Pergamon* **1995**, *33*, 1585–1592. [CrossRef]
43. Favvas, E.P.; Tsanaktsidis, C.G.; Sapalidis, A.A.; Tzilantonis, G.T.; Papageorgiou, S.K.; Mitropoulos, A.C. Clinoptilolite, a natural zeolite material: Structural characterization and performance evaluation on its dehydration properties of hydrocarbon-based fuels. *Microporous Mesoporous Mater.* **2016**, *225*, 385–391. [CrossRef]
44. Mansouri, N.; Rikhtegar, N.; Panahi, H.A.; Atabi, F.; Shahraki, B.K. Porosity, characterization and structural properties of natural zeolite-Clinoptilolite—As a sorbent. *Environ. Prot. Eng.* **2013**, *39*, 139–152. [CrossRef]
45. Uddin, M.T.; Rahman, M.A.; Rukanuzzaman, M.; Islam, M.A. A potential low cost adsorbent for the removal of cationic dyes from aqueous solutions. *Appl. Water Sci.* **2017**, *7*, 2831–2842. [CrossRef]
46. Zhang, S.; Wang, H.; Liu, J.; Bao, C. Measuring the specific surface area of monolayer graphene oxide in water. *Mater. Lett.* **2020**, *261*, 127098. [CrossRef]
47. Ho, Y.S.; McKay, G. Pseudo-second order model for sorption processes. *Process Biochem.* **1999**, *34*, 451–465. [CrossRef]
48. Suazo-Hernández, J.; Sans-Serramitjana, E.; Mora, M.d.l.L.; Fuentes, B.; Sepúlveda, M.d.L.Á.; Silva-Yumi, J.; Celletti, S.; Celi, L.; Rivas, S.; Ruiz, A. Assessment of the Effects of ZnO and CuO Engineered Nanoparticles on Physicochemical Properties of Volcanic Ash Soil and Phosphorus Availability. *Environments* **2024**, *11*, 208. [CrossRef]
49. Tene, T.; Guevara, M.; Valarezo, A.; Salguero, O.; Arias, F.A.; Arias, M.; Scarcello, A.; Caputi, L.S.; Gomez, C.V. Drying-time study in graphene oxide. *Nanomaterials* **2021**, *11*, 1035. [CrossRef]
50. Wu, F.C.; Tseng, R.L.; Juang, R.S. Initial behavior of intraparticle diffusion model used in the description of adsorption kinetics. *Chem. Eng. J.* **2009**, *153*, 1–8. [CrossRef]
51. Ma, Y.X.; Shao, W.J.; Sun, W.; Kou, Y.L.; Li, X.; Yang, H.P. One-step fabrication of β-cyclodextrin modified magnetic graphene oxide nanohybrids for adsorption of Pb(II), Cu(II) and methylene blue in aqueous solutions. *Appl. Surf. Sci.* **2018**, *459*, 544–553. [CrossRef]
52. Jaramillo-Fierro, X.; Cuenca, G. Enhancing Methylene Blue Removal through Adsorption and Photocatalysis—A Study on the GO/ZnTiO3/TiO2 Composite. *Int. J. Mol. Sci.* **2024**, *25*, 4367. [CrossRef]
53. Chu, H. Revisiting the Temkin Isotherm: Dimensional Inconsistency and Approximate Forms. *Ind. Eng. Chem. Res.* **2021**, *60*, 13140–13147. [CrossRef]
54. Algieri, V.; Tursi, A.; Costanzo, P.; Maiuolo, L.; De Nino, A.; Nucera, A.; Castriota, M.; De Luca, O.; Papagno, M.; Caruso, T.; et al. Thiol-functionalized cellulose for mercury polluted water remediation: Synthesis and study of the adsorption properties. *Chemosphere* **2024**, *355*, 141891. [CrossRef] [PubMed]

55. Al-Jubouri, S.M.; Al-Jendeel, H.A.; Rashid, S.A.; Al-Batty, S. Green synthesis of porous carbon cross-linked Y zeolite nanocrystals material and its performance for adsorptive removal of a methyl violet dye from water. *Microporous Mesoporous Mater.* **2023**, *356*, 112587. [CrossRef]
56. Hu, Q.; Zhang, Z. Application of Dubinin–Radushkevich isotherm model at the solid/solution interface: A theoretical analysis. *J. Mol. Liq.* **2019**, *277*, 646–648. [CrossRef]
57. Wu, M.; Li, Y.; Yue, R.; Zhang, X.; Huang, Y. Removal of silver nanoparticles by mussel-inspired Fe_3O_4 @ polydopamine core-shell microspheres and its use as efficient catalyst for methylene blue reduction. *Sci. Rep.* **2017**, *7*, srep42773. [CrossRef]
58. Su, H.; Li, W.; Han, Y.; Liu, N. Magnetic carboxyl functional nanoporous polymer: Synthesis, characterization and its application for methylene blue adsorption. *Sci. Rep.* **2018**, *8*, 6506. [CrossRef]
59. Gerçel, Ö.; Özcan, A.; Özcan, A.S.; Gerçel, H.F. Preparation of activated carbon from a renewable bio-plant of Euphorbia rigida by H_2SO_4 activation and its adsorption behavior in aqueous solutions. *Appl. Surf. Sci.* **2007**, *253*, 4843–4852. [CrossRef]
60. Wijaya, R.; Andersan, G.; Santoso, S.P.; Irawaty, W. Green Reduction of Graphene Oxide using Kaffir Lime Peel Extract (*Citrus hystrix*) and Its Application as Adsorbent for Methylene Blue. *Sci. Rep.* **2020**, *10*, 667. [CrossRef]
61. Saha, P.; Chowdhury, S. Insight Into Adsorption Thermodynamics. *Thermodynamics* **2011**, *16*, 349–364. [CrossRef]
62. Tursi, A.; Gallizzi, V.; Olivito, F.; Algieri, V.; De Nino, A.; Maiuolo, L.; Beneduci, A. Selective and efficient mercury(II) removal from water by adsorption with a cellulose citrate biopolymer. *J. Hazard. Mater. Lett.* **2022**, *3*, 100060. [CrossRef]
63. Lima, E.C.; Hosseini-Bandegharaei, A.; Moreno-Piraján, J.C.; Anastopoulos, I. A critical review of the estimation of the thermodynamic parameters on adsorption equilibria. Wrong use of equilibrium constant in the Van't Hoof equation for calculation of thermodynamic parameters of adsorption. *J. Mol. Liq.* **2019**, *273*, 425–434. [CrossRef]
64. Ghosal, P.S.; Gupta, A.K. Determination of thermodynamic parameters from Langmuir isotherm constant-revisited. *J. Mol. Liq.* **2017**, *225*, 137–146. [CrossRef]
65. Tene, T.; Arias, F.A.; Guevara, M.; Nuñez, A.; Villamagua, L.; Tapia, C.; Pisarra, M.; Torres, F.J.; Caputi, L.S.; Gomez, C.V. Removal of mercury(II) from aqueous solution by partially reduced graphene oxide. *Sci. Rep.* **2022**, *12*, 6326. [CrossRef] [PubMed]
66. Simonescu, C.M.; Simonescu, C.M.; Lavric, V.; Lavric, V.; Musina, A.; Musina, A.; Antonescu, O.M.; Antonescu, O.M.; Culita, D.C.; Culita, D.C.; et al. Experimental and modeling of cadmium ions removal by chelating resins. *J. Mol. Liq.* **2020**, *307*, 112973. [CrossRef]

Disclaimer/Publisher's Note: The statements, opinions and data contained in all publications are solely those of the individual author(s) and contributor(s) and not of MDPI and/or the editor(s). MDPI and/or the editor(s) disclaim responsibility for any injury to people or property resulting from any ideas, methods, instructions or products referred to in the content.